Monthly Notices of the ROYAL ASTRONOMICAL SOCIETY

MNRAS **533,** 4058–4067 (2024) https://doi.org/10.1093/mnras/stae1928
Advance Access publication 2024 August 8

Reconstructions of Jupiter's magnetic field using physics-informed neural networks

Philip W. Livermore [1,2] Leyuan Wu,[2,3]★ Longwei Chen[2,4]★ and Sjoerd de Ridder [1]

[1]*School of Earth and Environment, University of Leeds, Leeds LS2 9JT , UK*
[2]*Leeds Institute for Data Analytics, University of Leeds, Leeds LS2 9JT, UK*
[3]*Key Laboratory of Quantum Precision Measurement of Zhejiang Province, School of Physics, Zhejiang University of Technology, Hangzhou 310023, China*
[4]*Guangxi Key Laboratory of Exploration For Hidden Metallic Ore Deposits, College of Earth Sciences, Guilin University of Technology, Guilin 541006, China*

Accepted 2024 August 6. Received 2024 August 2; in original form 2024 July 11

ABSTRACT

Magnetic sounding using data collected from the Juno mission can be used to provide constraints on Jupiter's interior. However, inwards continuation of reconstructions assuming zero electrical conductivity and a representation in spherical harmonics are limited by the enhancement of noise at small scales. Here we describe new time-independent reconstructions of Jupiter's internal magnetic field based on physics-informed neural networks and either the first 33 (PINN33) or the first 50 (PINN50) of Juno's orbits. The method can resolve local structures, and allows for weak ambient electrical currents. Our models are not hampered by noise amplification at depth, and provide a smooth picture of the interior structure without explicit regularization. We estimate that the dynamo boundary is at a fractional radius of 0.8. At this depth, the magnetic field is arranged into longitudinal bands, and strong local features such as the great blue spot appear to be rooted in neighbouring structures of oppositely signed flux.

Key words: methods: numerical – planets and satellites: individual: Jupiter – planets and satellites: magnetic fields.

1 INTRODUCTION

The Juno mission, launched in 2011 (Bolton, 2010), has revolutionized our understanding of Jupiter's interior through the collection of both gravity and magnetic measurements in orbit since 2016. These new data have not only allowed new constraints on the density structure and zonal flow in the outermost parts of the planet (Kaspi et al. 2018; Militzer et al. 2022), but have permitted new reconstructions of the magnetic field to unprecedented resolution (e.g. Connerney et al. 2017, 2022). These magnetic maps highlight local features such as the great blue spot, sited within a large-scale hemispheric field (Moore et al. 2018) which shows evidence of secular variation (Ridley & Holme 2016; Moore et al. 2019; Bloxham et al. 2022; Connerney et al. 2022; Sharan et al. 2022), suggesting rich dynamics within the dynamo region (Bloxham et al. 2024).

In order to infer the structure of Jupiter's internally generated magnetic field, global reconstructions are needed that fit a physical model to the sparse magnetic data set collected on orbital trajectories. The physical model commonly adopted is that the data are measured within a region free of electrical currents, and comprise signals dominated by the internally generated field with more minor contributions from an external magnetic field and unmodelled instrumentation noise. Typical studies then proceed by subtracting an approximation to the external field assuming a magnetodisc structure, with estimates of the parameters (Connerney, Acuna & Ness 1981; Connerney et al. 2020), although the difficulty in adopting an accurate representation is compounded by its unknown, but likely, time-dependence (Ridley & Holme 2016; Moore et al. 2019). The remaining signal is then fit in a least-squares sense to an analytic description of an internally generated magnetic field $\mathbf{B}$, based on a potential V, with $\boldsymbol{B} = -\nabla V$. Any such magnetic field by construction exactly satisfies $\mathbf{J} = \mathbf{0}$, where $\mathbf{J} = \mu_0^{-1}\nabla \times \mathbf{B}$ is the ambient electrical current, and the constant μ_0 is the permeability of free space. Since the magnetic field is also divergence-free $\nabla \cdot \boldsymbol{B} = 0$, these two constraints together imply that $\nabla^2 V = 0$. The potential V is then represented in terms of solutions to Laplace's equation, namely spherical harmonics (truncated to degree N):

$$V = -R_J \sum_{n=0}^{N} \sum_{m=0}^{n} \left(\frac{R_J}{r}\right)^{n+1} P_n^m(\cos\theta) \times \left[g_n^m \cos(m\phi) + h_n^m \sin(m\phi)\right], \quad (1)$$

where g_n^m and h_n^m are the Gauss coefficients of degree n and order m, P_n^m are associated Legendre functions, and R_J is Jupiter's equatorial radius, 71 492km. Such a representation is the same as those used for comparable studies of Earth's magnetic field (e.g. Alken et al. 2021). Spherical harmonics are not only a natural mathematical basis for expansion, but they have additional useful properties such as orthogonality, uniform spatial resolution (Boyd 2001) and have a physical interpretation (for instance, the $l = 1$ modes represent the dipole component). Such spherical harmonic reconstructions allow not only spatial interpolation between the Juno measurements, but also extrapolation into regions unconstrained by measurements. Radially inwards (i.e. downwards) continuation under Jupiter's surface, assuming the same electrically insulating physics, is of particular interest because it allows inference of the

★ E-mail: leyuanwu@zjut.edu.cn (LW); longweichen_glut@glut.edu.cn (LC)

© 2024 The Author(s).
Published by Oxford University Press on behalf of Royal Astronomical Society. This is an Open Access article distributed under the terms of the Creative Commons Attribution License (http://creativecommons.org/licenses/by/4.0/), which permits unrestricted reuse, distribution, and reproduction in any medium, provided the original work is properly cited.

Downloaded from https://academic.oup.com/mnras/article/533/4/4058/7730260 by guest on 17 September 2024

dynamo radius, typical values for which are 0.8–0.83R_J (Connerney et al. 2022; Sharan et al. 2022).

However, the inverse procedure of inferring the magnetic field from the Juno measurements is ill-posed for two reasons. First is that due to the non-uniform sampling of magnetic field, some spherical harmonics (or linear combinations of harmonics) are better constrained than others; indeed, there is a large space of combinations of spherical harmonics that is unresolved by the Juno data (Connerney et al. 2022). Second is that inwards continuation using (1) involves a factor of $(R_J/r)^{n+2}$ for the spherical radial component of magnetic field, thus small-scale (large n) fields are amplified preferentially when evaluating the model at radii $r < R_J$. Because these small scales are often the least resolved due to leakage from unmodelled signals, inwards continuation can rapidly be swamped by noise.

There are a variety of ways proposed to fit the Gauss coefficients. The simplest is to truncate to low degree N, but there is often no objective way of choosing N. A common approach is to regularize the expansion, by fitting the coefficients in an optimization process that penalizes not only the spherical harmonic misfit but also the complexity of the model (e.g. Moore et al. 2018; Bloxham et al. 2022). This results in models which are principally large-scale, but with a subjective choice of the mathematical form and weighting of complexity. Lastly, the coefficients can be fit through a generalized singular value decomposition approach (Connerney 1981; Connerney et al. 2018, 2022), in which only those combinations of spherical harmonics that are resolvable by the data are retained, treating head-on the problem of data sparsity. However, because they are not explicitly regularized, they are unstable to inwards continuation.

In addition to the spherical harmonic methods described above best suited to represent global fields, other approaches have been proposed that are tailored for regional representations. Green's functions can connect a localized representation of magnetic field on a spherical grid to observations, regularizing either using an elastic net (Moore et al. 2017) or Subtractive Optimally Localized Averages (Hammer & Finlay 2019). Other approaches for localized magnetic field representation include Slepian functions (Beggan et al. 2013), wavelets (Holschneider, Chambodut & Mandea 2003), harmonic splines (Shure, Parker & Backus 1982), and spherical cap harmonics (Thébault, Schott & Mandea 2006).

In this paper, we propose a novel representation of Jupiter's internal magnetic field based on physics-informed neural networks (PINNs). Neural networks are mesh-free (that is, are not tied to any physical grid) and so offer a way of simultaneously representing both global and local features of a magnetic field. In this sense, our models offer an alternative hybrid approach between global spherical harmonics and localized models. Compared to spherical harmonic approaches, our models give a similar reconstruction on and above Jupiter's surface but appear to be more stable under inwards continuation. In the following sections, we first describe the data before outlining our PINN approach. We present our new reconstructions and estimates of the dynamo radius, which we compare with those from existing methods, and end with a brief discussion.

2 DATA

Our work is based on vector magnetic field measurements made by Juno within its first 50 perijoves during the period 2016 to 2023, which contains the prime mission of orbits 1–33. From these data we excluded the second perijove (PJ2) due to a spacecraft safe mode entry (Connerney et al. 2018). The original observations were down-sampled to a 30 s sampling rate, this being the approximate rotation time of the spacecraft, using a mean-value filter. At the small number of missing data points within each orbit, we average up to the missing data (even if less than 30 s) and restart our averaging after the missing data. In order to maximize the internal signal content of the data, we used only measurements recorded at planetocentric spherical radius $r \leq 4.0R_J$. The data likely lie within a current-free region, with external currents confined to a washer-shaped magnetodisc region (Connerney et al. 2020) with inner-radius about $8R_J$.

In total, there were 28 011 three-component measurements of the magnetic field, of periapsis 1.02 R_J and taking magnitudes ranging between approximately 6.5×10^4 to 16×10^5 nT. Fig. 1 shows an overview of the data used in this work.

3 PHYSICS-INFORMED NEURAL NETWORKS

3.1 Overview

PINNs offer a technique for spatial reconstruction by a neural network that is constrained not only by data but also physical laws (Raissi, Perdikaris & Karniadakis 2019; Karniadakis et al. 2021). They are based on multilayer perceptrons, feed-forward connected neural networks with multiple hidden layers, known to be universal approximators of any smooth function (Hornik, Stinchcombe & White 1989), including, as relevant to our case, both local and global magnetic fields. Unlike other purely data-driven methods in machine learning, PINNs are not simply trained on data but also are required to satisfy physical laws encapsulated by mathematical equations. In this sense, PINNs are interpretable in a similar way to other traditional numerical methods for solving PDEs because both satisfy the relevant physics. The application of PINNs in planetary magnetic field reconstruction is new, although recent related studies include magnetic imaging (Dubois et al. 2022), inference of magnetohydrodynamics within Earth's core (Li, Lin & Zhang 2024), mapping of magnetic fields in the solar corona (Jarolim et al. 2023), and modelling electromagnetic fluids (Mathews et al. 2021).

At the heart of the method is a neural network representation of the magnetic field, which is then fit to both data and physics constraints which are written in weak form (that is, fit by a penalization scheme but not enforced exactly). We work in a planetocentric Cartesian coordinate system, and write the magnetic field in terms of a vector-potential: $\boldsymbol{B} = \nabla \times \boldsymbol{A}$ which satisfies the fundamental relation $\nabla \cdot \boldsymbol{B} = 0$. The three independent components of $\boldsymbol{A}$, A_x, A_y, A_z, are expressed as individual feed-forward neural networks, each taking as input the position rescaled to $[-1, 1]^3$.

Each network is parametrized by the number of layers, the number of neurons per layer, and the choice of activation function. Symbolically each network can be written as a compound function

$$A_\alpha(\boldsymbol{r}) = (\mathcal{N}_\alpha^L \circ \mathcal{N}_\alpha^{L-1} \cdots \mathcal{N}_\alpha^0)(\boldsymbol{r}), \quad \alpha = x, y, z, \tag{2}$$

with the recursive definition

$$\begin{aligned} \text{input:} \quad & \mathcal{N}_\alpha^0(\boldsymbol{r}) = \boldsymbol{r}, \\ \text{hidden:} \quad & \mathcal{N}_\alpha^l(\boldsymbol{r}) = \sigma(\boldsymbol{W}_\alpha^l \mathcal{N}_\alpha^{l-1}(\boldsymbol{r}) + \boldsymbol{b}_\alpha^l), \quad 1 \leq l \leq L-1, \\ \text{output:} \quad & \mathcal{N}_\alpha^L(\boldsymbol{r}) = \boldsymbol{W}_\alpha^L \mathcal{N}_\alpha^{L-1}(\boldsymbol{r}) + \boldsymbol{b}_\alpha^L, \end{aligned} \tag{3}$$

where $\boldsymbol{r} = (x, y, z)$ are the input Cartesian coordinates (normalized to $[-1, 1]^3$), and $\boldsymbol{W}_\alpha^l$ and $\boldsymbol{b}_\alpha^l$ are weight matrices and bias vectors in the lth layer of the network. The function σ is the non-linear activation function.

We denote the set of tunable parameters (weights and biases) of the networks by $\boldsymbol{\Theta}$ and the representation of $\boldsymbol{A}$ as $\boldsymbol{A}_{\boldsymbol{\Theta}}(\boldsymbol{r})$. Because the

Downloaded from https://academic.oup.com/mnras/article/533/4/4058/7730260 by guest on 17 September 2024

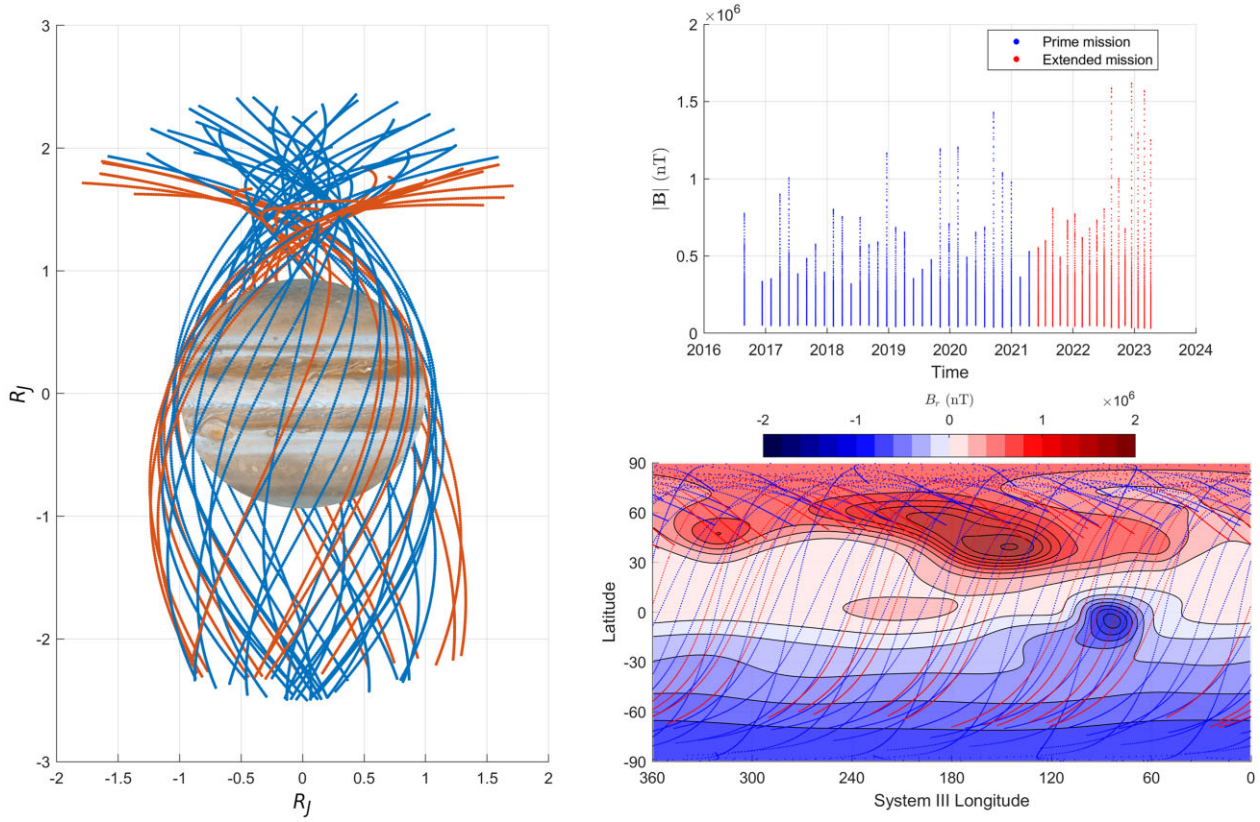

Figure 1. Illustration of Juno data used in this work. Left: Juno's global coverage after 50 orbits, showing Juno's trajectory within radius 2.5 R_J; the colours show the 33 prime mission orbits (blue lines) and the extended mission, orbits 34 onwards (red lines). Upper right: time span and magnitude range per orbit of Juno magnetic data within radius 2.5 R_J. Lower right: orbital position (radius within 2.5 R_J) projected on to a background contour map of the spherical radial component of magnetic field, B_r, at $r = R_J$ reconstructed using model PINN50e. Although we use data within radius 4 R_J in this paper, displaying only the data within radius 2.5 R_J highlights the measurements closest to Jupiter's surface for which the internal field signal dominates.

components of $\boldsymbol{A}_{\boldsymbol{\Theta}}(\boldsymbol{r})$ are continuous functions of position, they can be numerically differentiated (to machine precision) with respect to $\boldsymbol{r}$ using the chain rule, based on a technique called automatic differentiation (Baydin et al. 2018). In this way, quantities that are derived from the vector potential can be computed, namely $\boldsymbol{B}_{\boldsymbol{\Theta}}(\boldsymbol{r}) = \boldsymbol{\nabla} \times \boldsymbol{A}_{\boldsymbol{\Theta}}$ and $\boldsymbol{\nabla} \times \boldsymbol{B}_{\boldsymbol{\Theta}} = \boldsymbol{\nabla}(\boldsymbol{\nabla} \cdot \boldsymbol{A}_{\boldsymbol{\Theta}}) - \nabla^2 \boldsymbol{A}_{\boldsymbol{\Theta}}$.

A physics-informed model is trained by minimizing an objective function, which is a combination of loss terms describing the fit to the data and the equations describing the physics:

$$\mathcal{L}(\boldsymbol{\Theta}) = w_d \mathcal{L}_d(\boldsymbol{\Theta}) + w_p \mathcal{L}_p(\boldsymbol{\Theta}), \tag{4}$$

where $\mathcal{L}_d$ is the data loss and $\mathcal{L}_p$ is the physics loss. These terms are weighted by w_d and w_p, respectively. In our case, the data loss term is simply a sum over the squared difference between the neural network prediction of a magnetic field component and the observation itself; the physics loss is the squared summed magnitude of $\boldsymbol{\nabla} \times \boldsymbol{B}_{\boldsymbol{\Theta}}$ over a collocation grid:

$$\mathcal{L}_d(\boldsymbol{\Theta}) = \frac{1}{N_d} \sum_i^{N_d} |\boldsymbol{B}_{\boldsymbol{\Theta}}(\boldsymbol{r}_d^i) - \boldsymbol{B}(\boldsymbol{r}_d^i)|^2,$$

$$\mathcal{L}_p(\boldsymbol{\Theta}) = \frac{1}{N_p} \sum_i^{N_p} |(\boldsymbol{\nabla} \times \boldsymbol{B}_{\boldsymbol{\Theta}})(\boldsymbol{r}_p^i)|^2, \tag{5}$$

where N_p and $\boldsymbol{r}_p^i$ are the number and location of the collocation points used to constrain the physics loss, and N_d are the number of Juno data used, each of which has location $\boldsymbol{r}_d^i$ and vector value $\boldsymbol{B}(\boldsymbol{r}_d^i)$. We assume the contribution to the data loss from each measurement is equal for simplicity (following e.g. Bloxham et al. 2022), that is, each contribution to the sum is unweighted. We note that the data uncertainty is unlikely to be uniform across the observations but the only estimate of this error, that of the instrumentation range, likely underestimates the unmodelled signal error (Moore et al. 2017). We also make the assumption of equal contribution to the physics loss from each of the collocation points (although their clustering can effectively weight certain regions, see later discussion). We note that in the theoretical limit $w_p \to \infty$ in which the physics-loss is driven to zero, we would recover the spherical harmonic expansion of (1) in which the data were fit in a least-squares sense through $\mathcal{L}_d$. A schematic of the PINN is shown in Fig. 2.

In setting up our model, we have made various choices. First and most obvious is the structure of the network. Although we did not perform extensive hyperparameter tuning, we found that defining each neural network to have six hidden layers, 40 neurons per layer, and swish activation functions allowed us to represent Jupiter's magnetic field well with a data misfit comparable to other methods. The data misfit was larger with smaller networks, and larger networks did not improve the fit. A less obvious choice is the structure of the physics loss term. There are two constraints that the magnetic field should obey: $\boldsymbol{\nabla} \cdot \boldsymbol{B} = 0$ and $\boldsymbol{\nabla} \times \boldsymbol{B} = \boldsymbol{0}$. The first condition is a fundamental physical law, whereas the second is an approximation. We therefore opted to solve for a divergence-free

Downloaded from https://academic.oup.com/mnras/article/533/4/4058/7730260 by guest on 17 September 2024

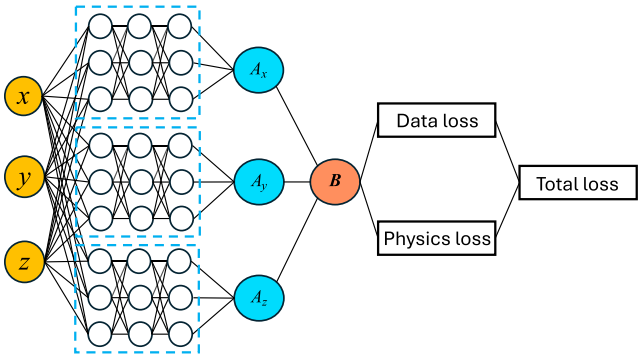

Figure 2. Schematic of the PINNs that we use. Three independent neural networks map position (x, y, z) to the three vector potential components. This in turn then defines $\boldsymbol{B}$ and consequently the data and physics loss, whose combination is minimized. Simplified neural networks are shown for illustration purposes with three layers (one hidden layer) and three neurons per layer.

vector field via a vector potential, and to then impose the zero-current constraint in weak form. This also means that any physics-loss residual can be physically interpreted as an electric current density. Alternative schemes could include solving for a curl-free magnetic field $\boldsymbol{B} = -\nabla V$ and then imposing $\nabla \cdot \boldsymbol{B} = 0$ in weak form, or imposing both physics constraints and the data fit in weak form to an otherwise arbitrary vector.

3.2 Training

The network parameters are found by minimizing the total loss $\mathcal{L}$. At each step of the descent algorithm, model parameters are updated according to

$$\boldsymbol{\Theta}^{(j+1)} = \boldsymbol{\Theta}^{(j)} - \eta^{(j)} \nabla_{\boldsymbol{\Theta}} \mathcal{L}(\boldsymbol{\Theta}^{(j)}), \quad j = 1, \cdots, N_T, \tag{6}$$

where the derivative of the combined loss function with respect to each of the parameter values, $\nabla_{\boldsymbol{\Theta}}\mathcal{L}$, is calculated using backpropagation (Baydin et al. 2018); $\eta^{(j)}$ is the learning rate at the jth iteration, and N_T is the total number of iterations. An empirical learning-rate annealing strategy is adopted where

$$\eta^{(j)} = 0.002 * 0.8^{j/1000}. \tag{7}$$

All neural network models are built with the machine learning framework TensorFlow (Abadi et al. 2016), and trained with the built-in Adam optimizer (Kingma & Ba 2015) over $N_T = 12\,000$ epochs with batch size 10 000.

To choose the weights and collocation points, we apply two techniques that improve the original method of Raissi et al. (2019): dynamic weights (Wang, Teng & Perdikaris 2021) and residual-based adaptive sampling of the collocation points (Wu et al. 2023).

The dynamic weights method introduced in Wang et al. (2021) is applied here to balance the gradients of physics and data loss terms during model training via back-propagation. A fixed value of $w_p = 1$ is chosen, while the value of w_d changes dynamically as

$$\begin{aligned} w_d^{(1)} &= 1, \\ \hat{w}_d^{(j)} &= \frac{\max\left(|\nabla_{\boldsymbol{\Theta}} \mathcal{L}_p|\right)}{\overline{|\nabla_{\boldsymbol{\Theta}} w_d^{(j)} \mathcal{L}_d|}}, \\ w_d^{(j+1)} &= \beta w_d^{(j)} + (1-\beta)\hat{w}_d^{(j)}, \quad j = 1, \cdots, N_T, \end{aligned} \tag{8}$$

where $\overline{|\nabla_{\boldsymbol{\Theta}} w_d^{(j)} \mathcal{L}_d|}$ denotes the mean absolute value of the gradients of the data loss term, and we use their recommended value of $\beta = 0.9$.

We also adopt residual-based sampling for the physics loss term. While uniformly sampled collocation points for the physics-based term offers a simple approach, recent studies have shown promising improvements in training accuracy by applying non-uniform adaptive sampling strategies (Lu et al. 2021; Nabian, Gladstone & Meidani 2021; Wu et al. 2023). Here we apply a simplified version of the residual-based adaptive distribution method described in Wu et al. (2023). For the first 3000 epochs we use a uniformly sampled set of points in a fixed region, but at epoch 3000 (and every 600 epochs thereafter) we create a probability density function $p(\boldsymbol{r})$, based on samples of the physics loss, which we use to resample the collaboration points, effectively increasing the local weighting in regions with a high physics loss. The PDF is defined as

$$p(\boldsymbol{r}) = A_\epsilon |\varepsilon(\boldsymbol{r})|^k, \tag{9}$$

with $\varepsilon(\boldsymbol{r})$ the physics loss at a collocation point at location $\boldsymbol{r}$, A_ϵ a normalizing constant, and we choose $k = 1$.

3.3 Key methodological differences

Having defined our approach, we take stock and highlight the key differences between our PINN representation and existing reconstructions based on a spherical-harmonic potential.

(i) Potential-based methods fit data in a weak form (by least squares) to physics imposed in a strong form (assuming an internal potential field representation with exactly zero electric current density). This is quite different in a PINN, where both data and physics are fit in a weak form, which makes them particularly effective in problems when the data and physics are imperfectly known (Karniadakis et al. 2021), as for Jupiter. Instead of assuming that $\boldsymbol{J} = 0$ and seeking a fit to an internally generated magnetic field, we penalize the mean-squared electrical current density $\boldsymbol{J}$ which allows, for example, weak non-zero electric currents if the data require them. We therefore allow for some uncertainty in the current-free approximation.

(ii) We do not (and indeed cannot) separate internal and external fields as we fit the PINN to the fundamental physical law, rather than to an analytic solution which assumes the location of source.

(iii) The spatial representation between the two approaches is quite different. A spherical harmonic representation, an analytic solution to Laplace's equation, is defined by a set of Gauss coefficients, whose globally resolved wavelength is approximately $2\pi/(N + 1/2)$, where N is the maximum degree (Backus, Parker & Constable 1996). In contrast, a neural network is a meshless method that has no physical grid, and can define both local and global solutions. It is defined by a set of weights and biases.

(iv) Spherical harmonic methods often require regularization; we do not use any explicit spatial regularization in our method. Although there is a curl in the physics loss which ostensibly penalizes small scales (due to the spatial derivative), actually the physics loss penalizes deviations from a potential field. Potential fields, satisfying exactly the physics constraint $\nabla \times \mathbf{B} = \mathbf{0}$, can have arbitrarily small lateral scales (by taking the spherical harmonic degree arbitrarily high). In our PINN, the only regularization is by our choice of network size.

Downloaded from https://academic.oup.com/mnras/article/533/4/4058/7730260 by guest on 17 September 2024

4 RESULTS

4.1 The PINN models

We create four time-independent PINN models, based on either the first 33 (PINN33i, PINN33e) or 50 Juno orbits (PINN50i, PINN50e). We deliberately distinguish between models internal to Jupiter (denoted by the character 'i') which inwards continue into $r \leq R_J$ the data observed in $r > R_J$, and those external to Jupiter (denoted by the character 'e') which interpolate data within the same exterior region in which Juno measurements are made $r > R_J$. Models PINN50e, PINN33e were made first, using 300 000 collocation points within the region $1 \leq r/R_J \leq 4$. Models PINN50i and PINN33i were then constructed, using 40 000 collocation points within the region $0.8 \leq r/R_J \leq 1$; for these models the data loss term was replaced by a term describing matching in all three vector components to either PINN50e or PINN33e on $r = R_J$ at 80 000 randomly located points. Although mildly oblate, Jupiter is assumed spherical for simplicity.

Fig. 3 illustrates the typical training diagnostics of our models as a function of epoch (i.e. iteration), here using the PINN50e model. The upper left panel shows the overall loss: dynamic loss refers to (4) with $w_p = 1$ and dynamic w_d; loss refers to (4) with $w_p = w_d = 1$ whose individual contributions are shown in the upper right panel. The dynamic weight w_d is shown in the lower left panel, with the learning rate in the lower right panel. From the (randomized) initial parameters, the loss decreases by about 10^3 in each component to a converged final state.

We now comment on model diagnostics, both in terms of the data loss and physics loss. Since both of these are defined external to Jupiter, we base our discussion on PINN33e and PINN50e. Fig. 4 shows the final data loss, in terms of an orbital comparison of the difference between the Juno data and four models: PINN33e, PINN50e, and two recent spherical harmonic models JRM33 ($N = 18$) (Connerney et al. 2022) and the Baseline model of Bloxham et al. (2022) with $N = 32$. These recent models have been chosen because although they are both based on the first 33 orbits, they differ in how the spherical harmonics are fitted: JRM33 uses an approach based on singular value decomposition, whereas the Baseline model uses regularization. Both of these studies adopt a magnetodisc approximation to the external field (Connerney et al. 2022) which we include alongside the spherical harmonic representation of the internal field; the PINN models represent both internal and external field. The models based only on the prime orbits (1–33, excluding 2): PINN33e, JRM33, and Baseline show a comparable absolute rms error per orbit. Noteably the PINN models do not achieve a much improved fit to the data, compared to JRM33 and Baseline,

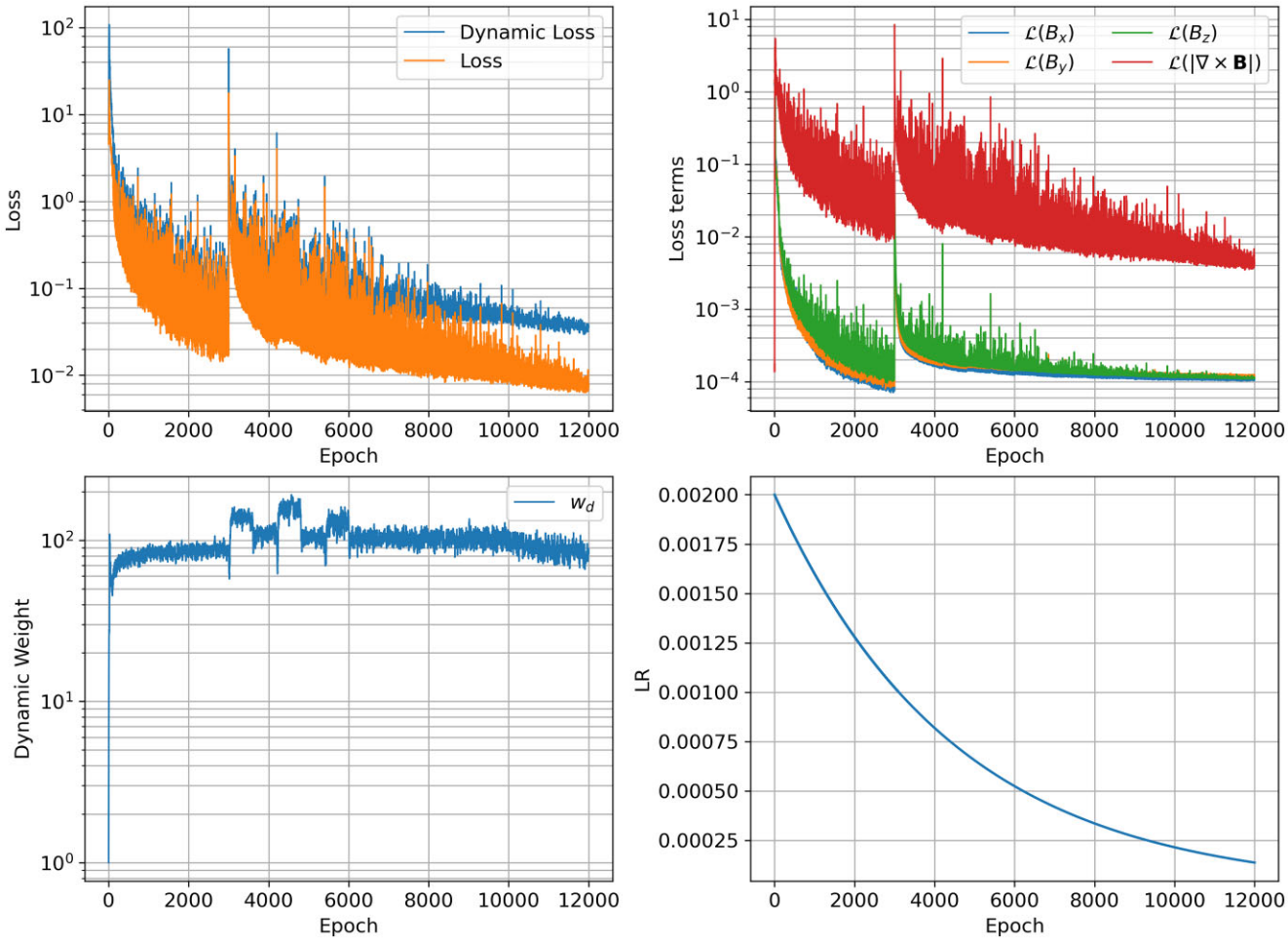

Figure 3. Training diagnostics from training model PINN50e. Upper left: comparison between mean squared dynamic and total loss; upper right: individual component contributions to the data loss and the physics loss. Lower left: the dynamic weight w_d as a function of training epoch; lower right: the learning rate.

Downloaded from https://academic.oup.com/mnras/article/533/4/4058/7730260 by guest on 17 September 2024

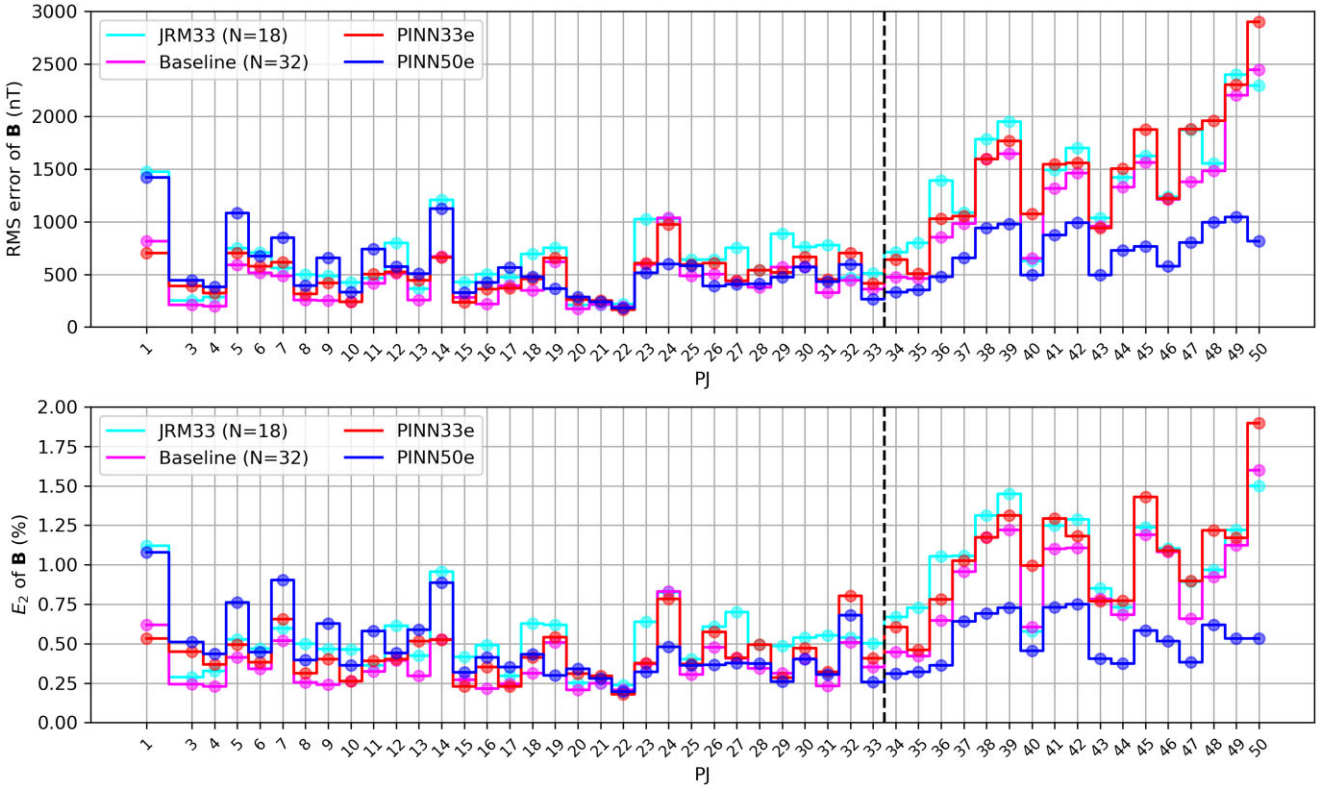

Figure 4. Orbital comparison of the discrepancy between various reconstructions of Jupiter's magnetic field: PINN33e, PINN50e, JRM33, and Baseline, with the Juno data. On each orbit, the error is quantified by taking the root mean squared value of the vector difference between the reconstructed magnetic field and the Juno measurements, similar to the data-loss term. We show the (upper) absolute value of this error, and (lower) relative value, E_2, of this error compared to the rms observed magnitude over the orbit. The dashed line delineates the prime from the extended mission.

despite being able to resolve an arbitrary external field. This suggests that the model misfit is dominated by unmodelled sources such as instrumentation error. For the majority of orbits, PINN33e has an error less than JRM33, with a few exceptions such as orbits 3 and 32. Over the first 33 orbits as a whole, the rms error for JRM33 is 680.5 nT, compared with 465.0 nT for Baseline and 519.7 nT for PINN33e. Applied to the data from orbits 34–50, these models exhibit a discrepancy with the measurements which grows with time, providing additional evidence for Jupiter's secular variation. Model PINN50e has a slightly higher rms error of 599.2 nT for orbits 1–33, but fits the data for orbits 34–50 much better because it has been trained in part on these data.

Fig. 5 shows the physics-loss by contours of the magnitude of electrical current density $|\mathbf{J}|$ on selected radii. For radii $r > R_J$, the magnitude of the current density of the PINN50e model is about 10^{-8} A m^{-2}, increasing with decreasing radius to about 10^{-6} A m^{-2} at $r = 0.8R_J$. The current density includes a signature from not only any external electrical currents, but also electromagnetic structures which are numerically favoured because they allow a good fit to the data. Estimates of the current density associated with a simple magnetodisc model are about 10^{-9}A m^{-2} at $r = 5R_J$ (Connerney 1981), which is consistent with our values in $r > R_J$. The increase of $|\mathbf{J}|$ by 100 from $r = 4$ to $r = 0.8$ is principally explained by the increase in magnetic field strength by a similar factor due to proximity to the dynamo source. Structurally, at large radii, $|\mathbf{J}|$ appears dominated by weak small-scale numerical artefacts; however, as the radius decreases, $|\mathbf{J}|$ becomes dominated by gradients in $\boldsymbol{B}$, focused at locations where the magnetic field is largest. The PINN models are not designed to satisfy $\boldsymbol{J} = \mathbf{0}$ everywhere, and we deem that the ambient currents are acceptably small.

We now use our models to image Jupiter's interior structure: we base our discussion on our PINN50i and PINN33i models which use the PINN methodology to inwards extrapolate. The structure of JRM33, Baseline, and PINN50i at radii $r/R_J = 1, 0.95, 0.9, 0.85, 0.8$ is shown by contours of radial field in Fig. 6. On $r = R_J$ the models are almost indistinguishable in terms of physical structure, but as the radius decreases, the magnetic field strength increases and the length-scales decrease. The instability of inwards continuation in the spherical harmonic models is readily apparent by the prevalent fine-scaled signal, particularly in the azimuthal direction. The (unregularized) JRM33 model in particular has a lot of small-scaled structure in the Southern hemisphere which is absent in the other smoother models. Although this signal is likely noise owing to the general instability of inwards continuation, we cannot rule out that in this specific case it actually represents resolved small-scale features due to the absence of any regularization. Of the three models, PINN50i is smoothest and remains relatively free of longitudinal small scales; consequently the features at depth are easier to identify. Of the three models, JRM33 has no spatial regularization at all, PINN50i has penalized physics and no explicit regularization, and the Baseline model is regularized through penalized horizontal derivatives of the radial field at $r = 0.9R_J$. We show the Baseline model at a range of radii although it is only regularized at a single radius; this is a different presentation to Moore et al. (2018) in which they show similar models but regularized on each specific radius shown. At $r = 0.9R_J$, the PINN50i model and Baseline show

Downloaded from https://academic.oup.com/mnras/article/533/4/4058/7730260 by guest on 17 September 2024

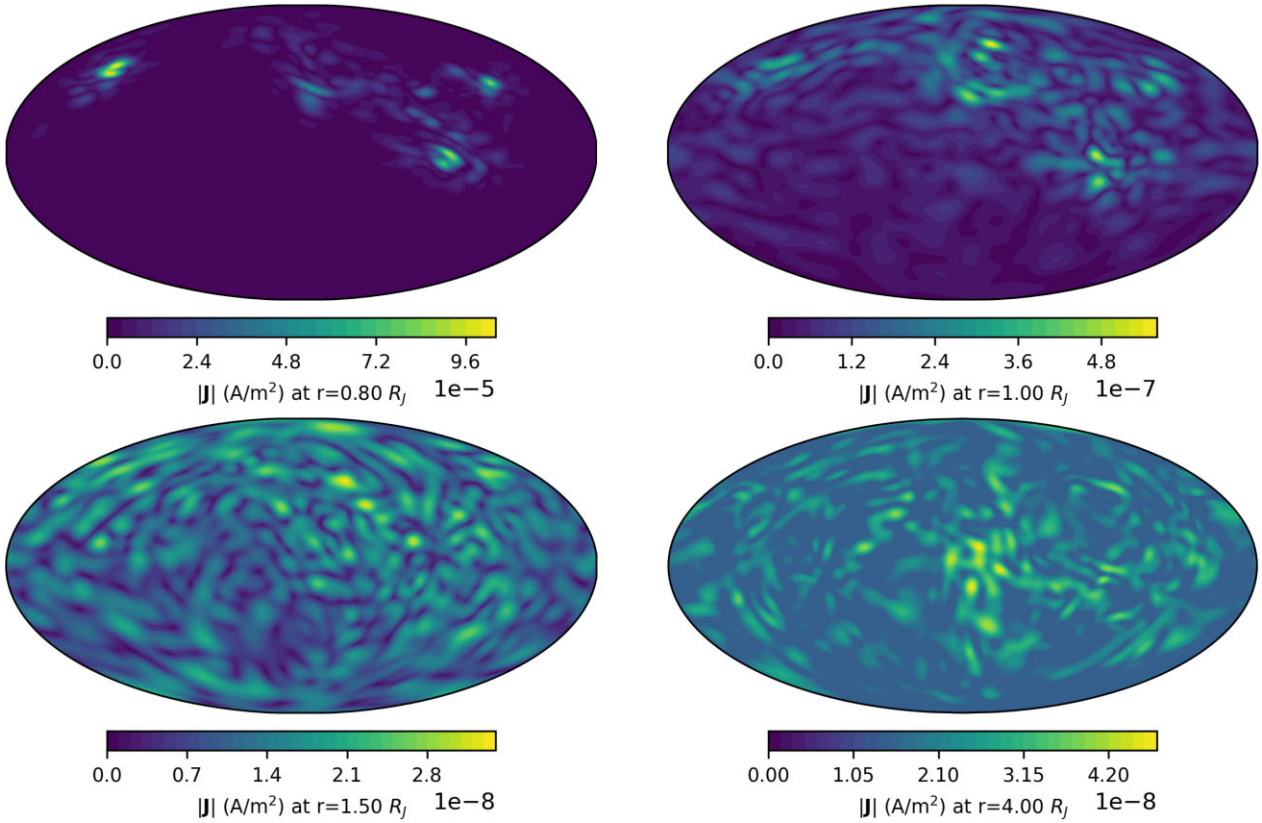

Figure 5. The magnitude of current density $|\mathbf{J}|$ from PINN50e and PINN50i shown on illustrative radii ($r/R_J = 0.8, 1, 1.5, 4$) on a Mollweide projection with the central meridian at a longitude of 180^o west (System III coordinates).

good agreement although there is still evidence of small scales in the Baseline model; the signature of these small scales increases beneath this radius.

At $r \leq 0.85R_J$, our PINN50i model indicates that the field is arranged into longitudinal bands of positive flux, with a strong band at high latitude and weaker bands near the equator. Many of the strong patches of flux have adjacent oppositely signed counterparts, as can be seen in particular around the root of the great blue spot. These reversed patches of magnetic field are also present in the Baseline model, and could either be a real feature or due to aliasing from the secular variation, recalling that our PINN models are time-independent over the Juno era. The hemispheric structure is also striking, with almost all the magnetic structure of the field being confined north of the equator.

4.2 Estimates of Jupiter's dynamo radius

Magnetic field reconstructions can be used to infer the location of the dynamo region, by identifying the radius at which the Lowes–Mauersberger spectrum of the magnetic field (Mauersberger 1956; Lowes 1974) is flat, assuming that the dynamo is a white-noise source of magnetic field. Although this assumption has been validated for Earth, it is not obviously applicable to giant planets, particularly as the smooth conductivity profiles (e.g. French et al. 2012) suggest that the edge of the dynamo is likely not as spatially abrupt as the core-mantle-boundary is in the Earth. Nevertheless, we use this simple diagnostic to compare the dynamo radius estimates from the PINN models with other recent models. Inference of the dynamo radius relies on the spherical harmonic representation of the magnetic field (1) from which the spectrum is derived as

$$R_n = (n+1)\left(\frac{R_J}{r}\right)^{(2n+4)} \sum_{m=0}^{n} (g_n^m)^2 + (h_n^m)^2, \tag{10}$$

whose profile with n depends on the radius r.

In the following text, we focus attention on the PINN50 models. In order to find the radius where the spectrum is flat, we have two options, noting that both involve extrapolating inwards away from the observed region ($r > R_J$). First is analytic continuation assuming exactly zero electrical current density, where we project the field at $r = R_J$ using PINN50e (or, equivalently PINN50i, because the models produce the same magnetic field at this radius) on to (1) and use the inherent radial dependence within (10). This approach is most similar to previous studies seeking to find the dynamo radius. Secondly, we can use PINN extrapolation based on the PINN50i model, in which the electrical current density is penalized but not forced to be zero. At each radius $r < R_J$, we project the magnetic field on to (1) and then use (10). In either case, we find the Gauss coefficients by performing a least-squares fit on to the internal field representation (1) using all three components of magnetic field and a dense spatial grid, which removes any external field contribution.

The upper part of Fig. 7 shows a comparison of the Gauss coefficients for the PINN50 model (either PINN50e or PINN50i), JRM33, and Baseline at $r = R_J$. They are all very similar at large-scales (small n, m), in accordance with the similarity of their physical

Downloaded from https://academic.oup.com/mnras/article/533/4/4058/7730260 by guest on 17 September 2024

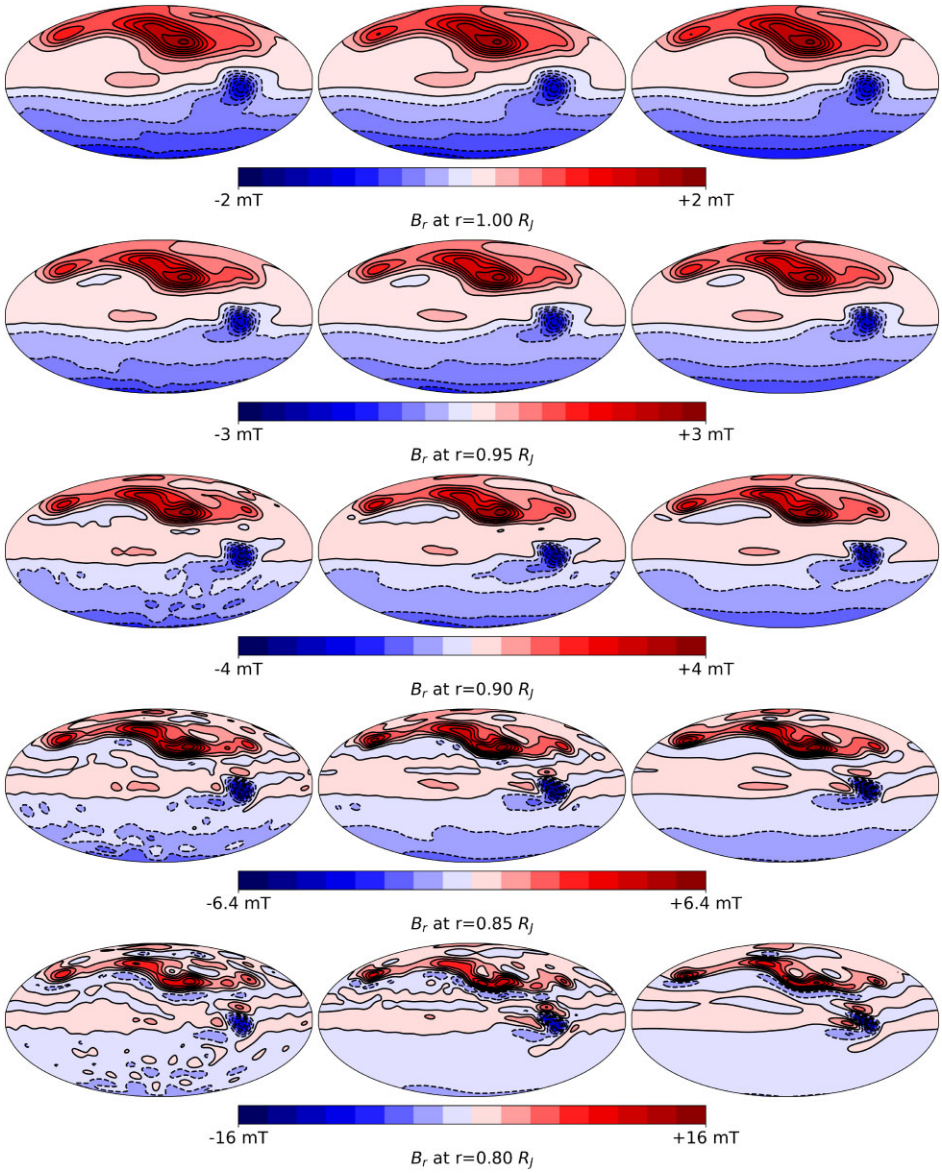

Figure 6. The radial component of Jupiter's magnetic field on various spherical radii inside Jupiter's surface. The plots are shown on a Mollweide projection with the central meridian at a longitude of 180^o west (System III coordinates). The left column shows the JRM33 model, $N = 18$ (Connerney et al. 2022), the middle column shows the Baseline model, $N = 32$ (Bloxham et al. 2022), and the right column shows the model PINN50i.

representation at $r = R_J$ (Fig. 6). The spherical harmonic model JRM33, with no regularization, has higher power at small scales $(n, m \geq 20)$ than the other two models. The PINN50 model has no explicit regularization either, but small-scale features appear to be penalized with a noteable decrease in power at small scales $n, m \geq 20$, somewhat mirroring the result of the explicit damping applied in the Baseline model.

The middle panel of Fig. 7 shows the Lowes–Mauersberger spectrum as a function of degree n for JRM33, Baseline, PINN50e (coloured lines: analytic continuation), and PINN50i (black symbols: PINN extrapolation). The maximum degree of 35 for the PINN models is chosen arbitrarily, with the representation of the PINN models in terms of spherical harmonics achieved using least squares projection as described above. At $r = R_J$ the spectral power for degrees 2–18 agrees well between the models and falls off exponentially with n. The power in the dipole is higher than a simple profile predicts. As the radius is decreased the profile flattens as the smaller scales become more prominent. Above degree 18, the three analytically continued models diverge, with JRM33 having the most power at high degree. Of the three models, the Baseline model (which is the only model with explicit regularization) has the least power at small-degree. Comparing the analytic and PINN extrapolation methods, although they agree on $r = R_J$ by construction, for $r < R_J$ and degrees higher than about 18 they diverge, with the PINN extrapolated models having smaller power at high degree.

We quantify the slope of the spectrum by fitting a straight line to $\log_{10} R_n$ for degrees 2–18. The lower panel of Fig. 7 shows the slope variation with radius for four models analytically inwards continued using (10); the extrapolated PINN models give very similar results. On making the assumption that the slope is zero at the source we infer that the dynamo radius is about $r = 0.8R_J$, in approximate

Downloaded from https://academic.oup.com/mnras/article/533/4/4058/7730260 by guest on 17 September 2024

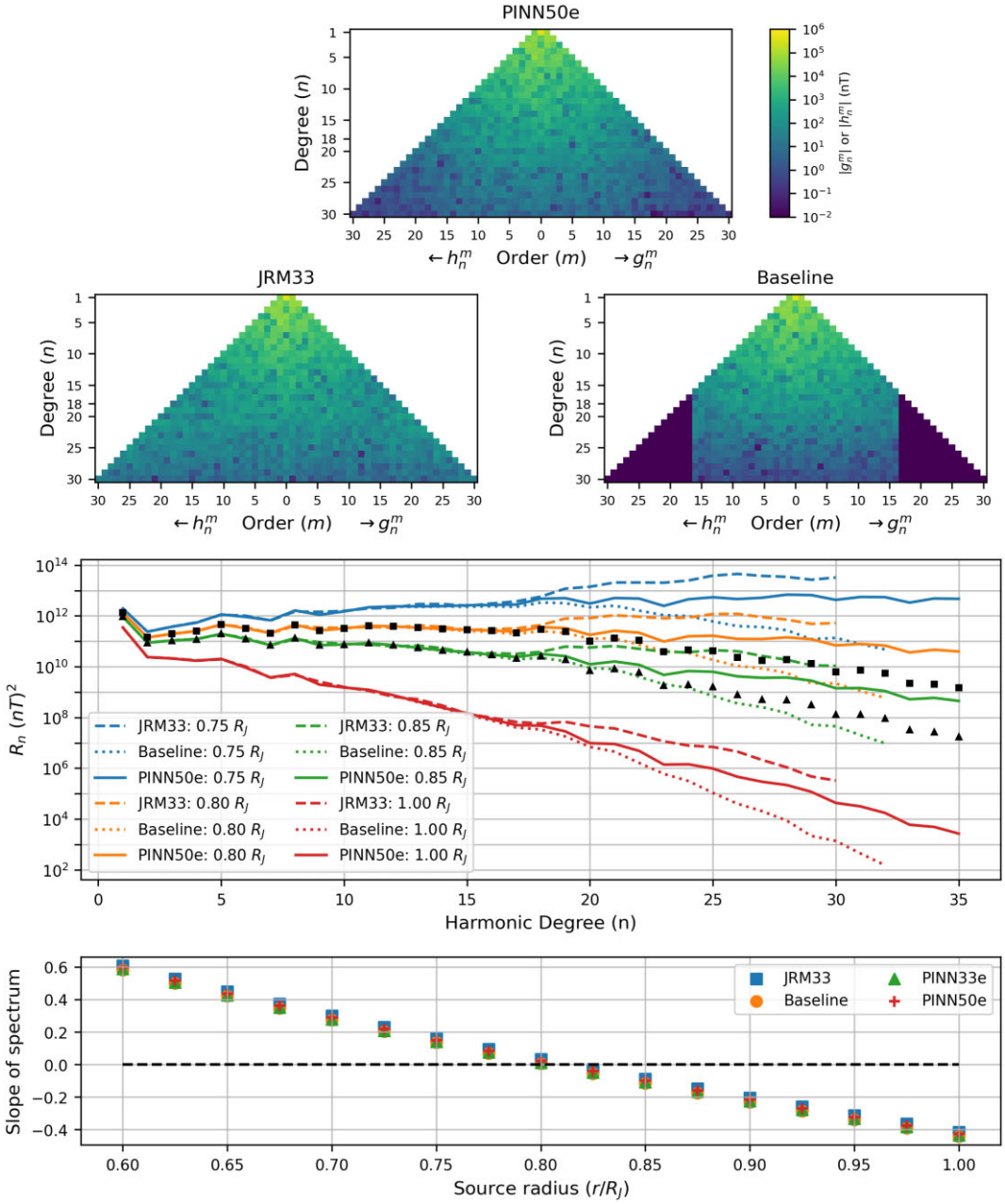

Figure 7. Upper panel: Gauss coefficients of PINN50e/i at $r = R_J$, JRM33, and Baseline. Middle panel: Lowes–Mauersberger spectrum of three inwards analytically continued models (coloured lines): PINN50e ($N = 35$), JRM33 ($N = 30$), and Baseline ($N = 32$); the black symbols show similar spectra obtained from PINN extrapolation using PINN50i in $r < R_J$ (squares: $0.80R_J$; triangles: $0.85R_J$). Lower panel: spectral slope (fit to degrees 2–18) with radius for four analytically continued models: JRM33, Baseline, PINN33e, and PINN50e.

agreement with other studies (e.g. Connerney et al. 2022; Sharan et al. 2022).

5 DISCUSSION AND CONCLUSIONS

We have presented reconstructions of Jupiter's magnetic field, based on data from Juno within the framework of a PINN. Our reconstructions have a similar misfit to the data compared with other spherical harmonic methods, and produce a similar structure of magnetic field on Jupiter's surface. However, using a meshless method, and only weakly constraining the (poorly known) physics, our models are not apparently hostage to the typically enhanced noise with decreasing radius despite not using any explicit spatial regularization. This is possible because the PINN allows unmodelled signal to be mapped to (arguably unphysical but small) electrical currents rather than to the internal field, stabilizing inwards continuation. Compared with spherical harmonic-based methods, we produce a smoother image at depth of the localized interior magnetic field, making specific features easier to identify and interpret. We do not claim however that our models are more accurate than other reconstructions, as there is no physics-based justification for preferring smoother models over more complex models.

The fact that most of the structure in Jupiter's field appears confined to the Northern hemisphere perhaps makes neural networks

Downloaded from https://academic.oup.com/mnras/article/533/4/4058/7730260 by guest on 17 September 2024

a particularly effective modelling tool. Even at modest resolution, neural networks are able to very well represent local structures, compared to spherical harmonics which are inherently global. Future applications of the PINN method include quantifying the secular changes close to Jupiter's dynamo region, and applications to other planets.

ACKNOWLEDGEMENTS

This study was funded by the National Natural Science Foundation of China (Grant No. 42474184, 42374173), and National Natural Science Foundation of Guangxi Province of China (Grant No. 2020GXNSFDA238021). This work was undertaken on ARC4, part of the High Performance Computing facilities at the University of Leeds, UK. We thank Jack Connerney for help with accessing the Juno data. The Jupiter image in figure 1 was produced using the planet3D tool https://github.com/tamaskis/planet3D-MATLAB.

DATA AVAILABILITY

The Juno magnetometer data are publicly available on NASA's Planetary Data System (PDS) at https://pds.nasa.gov/. The produced PINN models, together with input processed Juno data, spherical harmonic models, and all related Python code and Jupyter notebooks to reproduce all the results in this work are archived in the Github repository https://github.com/LeyuanWu/JunoMag_PINN_VP3.

REFERENCES

Abadi M. et al., 2016, in Proc. OSDI 16, 265
Alken P. et al., 2021, Earth Planets Space, 73, 1
Backus G., Parker R. L., Constable C., 1996, Foundations of Geomagnetism. Cambridge Univ. Press, Cambridge
Baydin A. G., Pearlmutter B. A., Radul A. A., Siskind J. M., 2018, J. Mach. Learn. Res., 18, 153
Beggan C. D., Saarimäki J., Whaler K. A., Simons F. J., 2013, Geophys. J. Int., 193, 136
Bloxham J., Moore K. M., Kulowski L., Cao H., Yadav R. K., Stevenson D. J., Connerney J. E., Bolton S. J., 2022, J. Geophys. Res., 127, e2021JE007138
Bloxham J., Cao H., Stevenson D. J., Connerney J. E., Bolton S. J., 2024, Nature, 627, 64
Bolton S., 2010, in Barbieri C., Chakrabarti S., Coradini M., Lazzarin M., eds., Proceedings of the International Astronomical Union, Galileo's Medicean Moons: their impact on 400 years of discovery, Cambridge University Press, 6, 92
Boyd J. P., 2001, Chebyshev and Fourier Spectral Methods. Dover, New York
Connerney J. E. P., 1981, J. Geophys. Res., 86, 7679
Connerney J. E. P., Acuna M. H., Ness N. F., 1981, J. Geophys. Res., 86, 8370
Connerney J. E. P. et al., 2017, Space Sci. Rev., 213, 39
Connerney J. E. P. et al., 2018, Geophys. Res. Lett., 45, 2590
Connerney J. E. P., Timmins S., Herceg M., Joergensen J. L., 2020, J. Geophys. Res., 125, e2020JA028138
Connerney J. E. P. et al., 2022, J. Geophys. Res., 127, e2021JE007055
Dubois A. E. et al., 2022, Phys. Rev. Appl., 18, 064076
French M., Becker A., Lorenzen W., Nettelmann N., Bethkenhagen M., Wicht J., Redmer R., 2012, ApJS, 202, 5
Hammer M. D., Finlay C. C., 2019, Geophys. J. Int., 216, 1901
Holschneider M., Chambodut A., Mandea M., 2003, Phys. Earth Planet. Inter., 135, 107
Hornik K., Stinchcombe M., White H., 1989, Neural Netw., 2, 359
Jarolim R., Thalmann J., Veronig A., Podladchikova T., 2023, Nat. Astron., 7, 1171
Karniadakis G. E., Kevrekidis I. G., Lu L., Perdikaris P., Wang S. F., Yang L., 2021, Nat. Rev. Phys., 3, 422
Kaspi Y. et al., 2018, Nature, 555, 223
Kingma D. P., Ba J., 2015, Adam: A Method for Stochastic Optimization., Proceedings of the 3rd International Conference on Learning Representations (ICLR 2015), available at http://arxiv.org/abs/1412.6980
Li J., Lin Y., Zhang K., 2024, Geophys. Res. Lett., 51, e2023GL106362
Lowes F., 1974, Geophys. J. Int., 36, 717
Lu L., Meng X. H., Mao Z. P., Karniadakis G. E., 2021, SIAM Rev., 63, 208
Mathews A., Francisquez M., Hughes J. W., Hatch D. R., Zhu B., Rogers B. N., 2021, Phys. Rev. E, 104, 025205
Mauersberger P., 1956, Gerlands Beitr. Geophys., 65, 207
Militzer B. et al., 2022, Plan. Sci. J., 3, 185
Moore K. M., Bloxham J., Connerney J. E. P., Jorgensen J. L., Merayo J. M. G., 2017, Geophys. Res. Lett., 44, 4687
Moore K. M. et al., 2018, Nature, 561, 76
Moore K. M., Cao H., Bloxham J., Stevenson D., Connerney J., Bolton S., 2019, Nat. Astron., 3, 730
Nabian M. A., Gladstone R. J., Meidani H., 2021, Comput.-Aided Civ. Infrastruct. Eng., 36, 962
Raissi M., Perdikaris P., Karniadakis G. E., 2019, J. Comput. Phys., 378, 686
Ridley V. A., Holme R., 2016, J.Geophys. Res., 121, 309
Sharan S., Langlais B., Amit H., Thebault E., Pinceloup M., Verhoeven O., 2022, Geophys. Res. Lett., 49, e2022GL098839
Shure L., Parker R. L., Backus G. E., 1982, Phys. Earth Planet. Inter., 28, 215
Thébault E., Schott J., Mandea M., 2006, J. Geophys. Res., 111, B01102
Wang S. F., Teng Y. J., Perdikaris P., 2021, SIAM J. Sci. Comput., 43, A3055
Wu C. X., Zhu M., Tan Q. Y., Kartha Y., Lu L., 2023, Comput. Methods Appl. Mech. Eng., 403, 115671

This paper has been typeset from a TEX/LATEX file prepared by the author.

Downloaded from https://academic.oup.com/mnras/article/533/4/4058/7730260 by guest on 17 September 2024

© 2024 The Author(s).
Published by Oxford University Press on behalf of Royal Astronomical Society. This is an Open Access article distributed under the terms of the Creative Commons Attribution License (http://creativecommons.org/licenses/by/4.0/), which permits unrestricted reuse, distribution, and reproduction in any medium, provided the original work is properly cited.